Microsyst Technol
DOI 10.1007/s00542-015-2504-9

TECHNICAL PAPER

Preliminary mechanical analysis of an improved amphibious spherical father robot

Yanlin He[1,2] · Liwei Shi[1,2] · Shuxiang Guo[1,2,3] · Shaowu Pan[1,2] · Zhe Wang[1,2]

Received: 15 March 2015 / Accepted: 18 March 2015

Abstract Amphibious micro-robots are being developed for complicated missions in limited spaces found in complex underwater environments. Therefore, compact structures able to perform multiple functions are required. The robots must have high velocities, long cruising times, and large load capacities. It is difficult to meet all these requirements using a conventional underwater micro-robot, so we previously proposed an amphibious spherical father–son robot system that includes several micro-robots as son robots and an amphibious spherical robot as a father robot. Our father robot was designed to carry and power the son robots. This paper discusses improvements to the structure and mechanism of the father robot, which was designed to have a spherical body with four legs. Based on recent experiments in different environments, we have improved the father robot by adding four passive wheels, and we have redesigned its structure by means of three-dimensional printing technology, resulting in greatly improved velocity and stability. Moreover, due to the complexity and uncertainty of many underwater environments, it is essential for the father robot to have adequate structural strength. We analyzed the movement mechanisms and structural strength using finite element analysis to obtain the deformation and equivalent stress distributions of the improved robot. The results provide support for further analysis of the structural strength and optimal design of our amphibious spherical father robot.

1 Introduction

In recent years, considerable underwater robotics research has focused on manipulating sophisticated systems for inspecting and maintaining underwater structures, which can include cluttered and complex areas such as narrow clear spaces. These robots may be used for feature and cable tracking, deep-ocean exploration, and to carry out tasks in environments full of coral reefs (Zhang et al. 2004; Mori and Hirose 2006). Many researchers have focused on downsizing their robots by optimizing their structures and employing smaller motors (Ha and Goo 2010; Wang et al. 2011). However, traditional motor-actuated robots have challenges related to their limits in size and the power consumption of their motors. Consequently, smart actuators are being used to develop micro-robots (Chen et al. 2010; Villanueva et al. 2010). Smart actuators are usually simple and light, and some of them have low power consumption, leading to various new small robots and new movement methods. These actuators include ionic polymer metal composite (IPMC) and smart memory alloy (SMA) actuators (Brunetto et al. 2008; Abdulsadda and Tan 2012; Shi et al. 2011, 2012a, 2012b, 2013a; Guo et al. 2012a). In our previous research, we developed a micro-robot utilizing two IPMC actuators and a short-range proximity sensor. We also designed an electronic mechanical model to evaluate the grasping ability of a robot using different voltages, and added eight bio-mimetic IPMC legs to implement walking and rotating motion (Shi et al. 2012b, 2013c).

✉ Liwei Shi
shiliwei@bit.edu.cn

[1] The Institute of Advanced BioMedical Engineering System, School of Life Science, Beijing Institute of Technology, No. 5, Zhongguancun South Street, Haidian District, Beijing, China

[2] Key Laboratory of Convergence Medical Engineering System and Healthcare Technology, the Ministry of Industry and Information Technology, Beijing Institute of Technology, No. 5, Zhongguancun South Street, Haidian District, 100081 Beijing, China

[3] Faculty of Engineering, Kagawa University, 2217-20 Hayashi-cho, Takamatsu, Kagawa, Japan

Published online: 19 April 2015

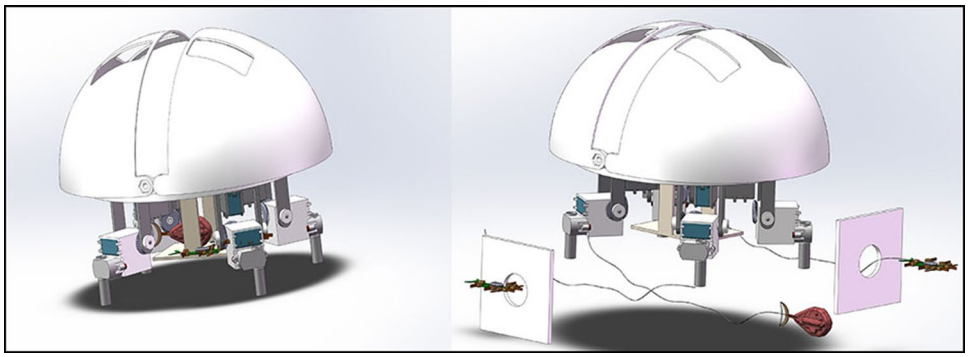

Fig. 1 Amphibious *spherical* father–son robot system

However, although many advances have been made in the field of micro-robotics, robots cannot yet be applied to practical situations for the following reasons (Behkam and Sitti 2006; Zhang et al. 2006; Heo et al. 2007; Wang et al. 2008; Liu et al. 2010; Najem et al. 2012). First, the movement range of micro-robots is too short. Second, micro-robots cannot access a relatively stable power supply. Third, it is difficult to develop an intelligent micro-robot or to have multiple robots interact and cooperate due to their size. To resolve these problems, we proposed a father–son robot system to provide an effective alternative to existing robots. This system includes several micro-robots, which are used as son robots, and an amphibious spherical robot, which is used as a father robot. The father robot, which acts as a base station, carries and controls several son robots, as shown in Fig. 1. To complete a task, the father robot carries the micro-robots to the desired position and stabilizes itself, and then the micro-robots walk or swim out of the father robot on land or in water. With this father–son robot system, it is possible to use cable control between the father robot and the micro-robots due to the short distance between them, allowing the father robot to provide power to the micro-robots and to control them. Thus, the micro-robots can be designed to be more compact and flexible.

A spherical robot has good water resistance, and is it easy to realize a zero turning radius regardless of the state of motion (Lin et al. 2010; Lin and Guo 2012; Li et al. 2014). Inspired by an amphibious turtle, our father robot was designed with one hemisphere body, two quarter-spherical hulls, and four legs with two degrees of freedom (DOFs). Further details about our father robot are provided in Sect. 2. Experiments using our proposed amphibious spherical father–son robot system have previously demonstrated the rationality and effectiveness of our structural design. However, we also discovered some problems; for example, the walking velocity of the father robot on level or comparatively smooth terrain was slow, and its stability and reliability needed improvement. We undertook several improvements to solve these problems. First, we added four passive wheels to the bottom of the father robot's legs to improve its walking velocity on level or comparatively smooth terrain (Shi et al. 2013d). Second, we redesigned the overall structure of the father robot and changed the method of assembling the robot using three-dimensional (3D) printing technology (He et al. 2014). We conducted some test experiments on a flat desk; the results demonstrated the practicality of our redesign, and revealed minimal instability. We used the finite element method to analyze the structure of the father robot, and examined the deformation of the hemispherical robot shell in different water depths. We then proceeded with a mechanical analysis. This provided the basis for an optimal design.

The remainder of this paper is organized as follows. First, we briefly introduce our amphibious spherical father–son robot system. Second, we describe the analysis and testing of the father robot, with a focus on experimental verification of its structural strength and overall feasibility. We then present our conclusions.

2 Review of the amphibious spherical father robot

2.1 Previous design

Inspired by an amphibious turtle, our amphibious spherical father robot has a spherical body with four legs. It uses amphibious motions to extend the range of the son robots. A spherical structure can rotate and change its direction more easily than a traditional streamlined structure, while providing a relatively large interior space to hold the son micro-robots (Guo et al. 2012b; Shi et al. 2013b). As shown in Fig. 2, our previously proposed amphibious spherical father robot is composed of one hemisphere, two quarter-spherical hulls, and four legs. Each leg is actuated by two servomotors and one water-jet propeller. The two servomotors are installed at right angles in the horizontal and vertical planes. Each water-jet propeller can be rotated by the two servomotors so that the direction of the water-jet thruster can be changed in the horizontal or vertical plane. The two quarter-spherical hulls can be actuated by another two servomotors, allowing them to open or close.

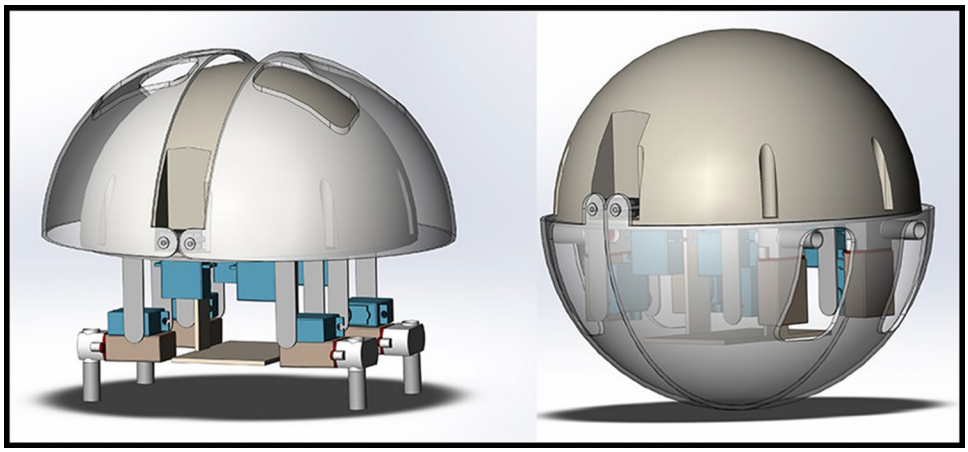

Fig. 2 Appearance of the amphibious spherical father robot (Guo et al. 2012b)

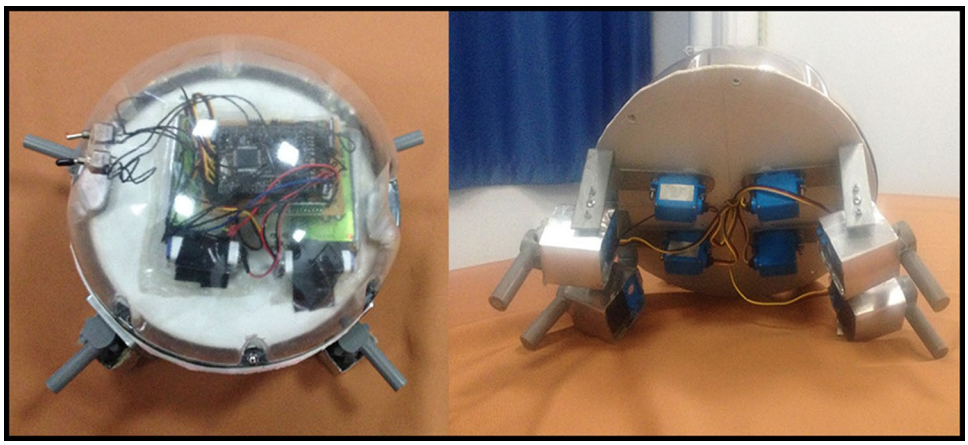

Fig. 3 Prototype of the father robot

The proposed amphibious spherical father robot can walk on a cement floor, paving stones, and grass, or in shallow water. The following procedure is used to take a step. First, the servomotor installed in the vertical plane rotates to lift up the water-jet propeller. Second, the servomotor installed in the horizontal plane actuates the water-jet propeller to swing forward. Third, the water-jet propeller drops down. Last, it swings backward to complete the step. By changing the gait of the four legs, the robot can walk and rotate with different velocities. Different motions are possible in an underwater environment. By changing the directions and propulsive forces of the four vectored propellers, the robot can complete forward or backward motion, rotate clockwise or counter-clockwise, execute a surface/diving motion, and remain still in an underwater environment (Guo et al. 2012b; Shi et al. 2013b).

As illustrated in Fig. 3, the prototype of our amphibious spherical father robot consists of one hemisphere body, two quarter-spherical hulls, and four legs with two DOFs. The diameter of the hemispherical shell is 234 mm, and that of the two symmetrical quarter-spherical hulls is 250 mm. The thickness of the hemispherical shell and the two quarter-spherical hulls are the same: 3 mm. Six small grooves are used to accommodate the bolts and nuts, and two large grooves are used for the servomotors used to open the two quarter-spherical hulls. The total weight of the amphibious spherical father robot is approximately 1.41 kg. The microprocessor unit is an ATmega2560. The microprocessor unit, motor-driving circuits, and power supply module are fixed and sealed in the hemispherical shell (Shi et al. 2013b).

2.2 Evaluation experiments and conclusions

We conducted experiments on a flat floor to evaluate the walking performance of our proposed amphibious spherical father robot while it is working on land. Figure 4 presents photographs of the robot walking: the robot achieves perfect walking motion on cement floors, paving stones, and grass, or in shallow water. Inspired by the walking motion of an amphibious turtle, the robot adopts a crawling gait to enhance stability; this is a statically stable regular symmetric gait. Different timing sequences can result in different gaits, as shown in Fig. 5. The time required to complete one full cycle is defined as 1 unit. The black bars indicate the time intervals when the legs touch the ground to support the robot; the white bars correspond to periods when

Fig. 4 Walking motion of the father robot

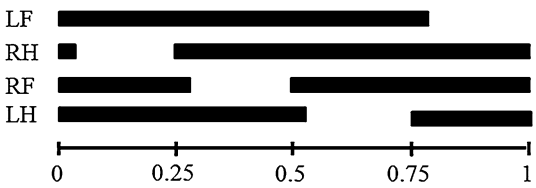

Fig. 5 Event sequences of the crawl gait (Shi et al. 2013b)

the legs are lifted up and do not touch the ground. In the walking actuation mode, the water-jet motors are used as legs; each actuating unit can realize a stepping forward or stepping backward motion. The timing sequence of the four actuation units must be synchronized to achieve a quadruped walking motion. As shown in Fig. 5, three or four legs always touch the ground to support the robot and ensure that it remains stable (Guo et al. 2012b).

The duty factor and relative phases of the legs are critical parameters for the gait. To ensure that three or four legs are always supporting the robot, the duty factor must be at least 0.75. In our case, the duty factor was set to 0.80. Each leg lags another leg by 0.25 in the following sequence: left front leg—right hind leg—right front leg—left hind leg.

We conducted experiments to evaluate the performance of the amphibious spherical father robot in an underwater environment. As shown in Fig. 6, the robot can realize three DOFs while moving underwater by using the water-jet mechanism: horizontally moving forward, rotating, and vertically moving up and down. For vertical movement, the water-jet direction is adjusted to generate the desired actuating force. When moving down, the water-jet motor turns 120° and jet water generates the actuating force in the opposite direction to avoid a collision between the water jet and the upper hemisphere of the robot. The water-jet motor is deployed horizontally for horizontal movement. By turning the appropriate water-jet motors on and off, the amphibious spherical father robot can move forward and turn (Guo et al. 2012b).

3 Structural optimization of the father robot

3.1 Structural details

We previously encountered some problems with our father robot. For example, the robot could not maintain a stable state for a long period of time while walking on land or swimming underwater, its reliability was not sufficiently high, its fatigue life was too short, and it was not sufficiently waterproof. Thus, the overall structural design needed to be improved. Also, its joints were not perfect: it encountered some unexpected phenomena while walking, such as leg buckling caused by a loose screw. To solve these problems, we used 3D printing technology to fabricate our new father robot, and we attempted to integrate the design and ensure seamless connections between the parts to reduce the volatility of the walking process and increase the stability. Three-dimensional printing technology avoids introducing manual errors during fabrication, maximizes the use of the upper spherical hemispherical space and resources, and makes the overall appearance of the robot more compact and aesthetically pleasing.

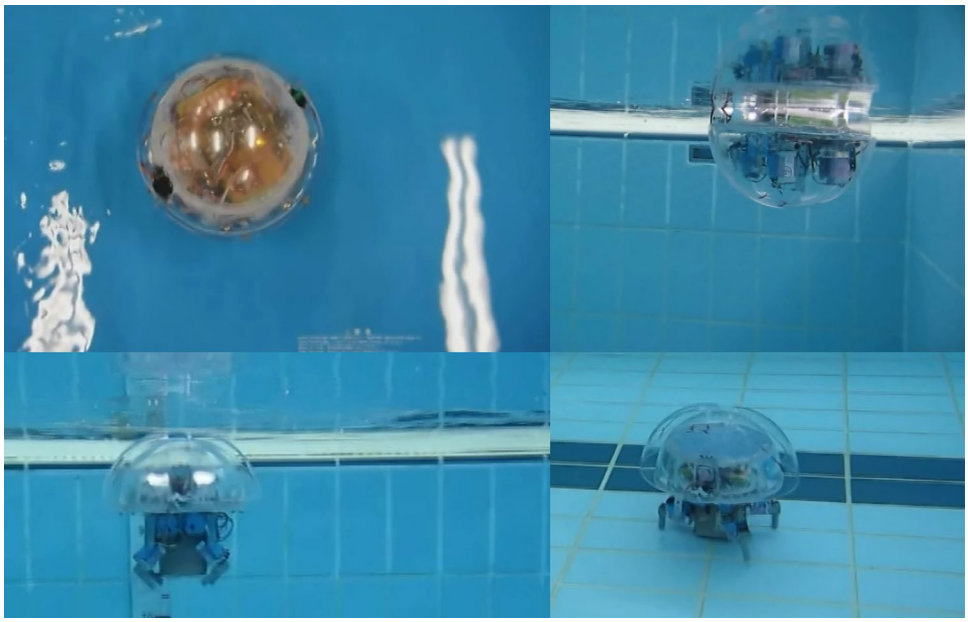

Fig. 6 Underwater motion of the father robot (Shi et al. 2013b)

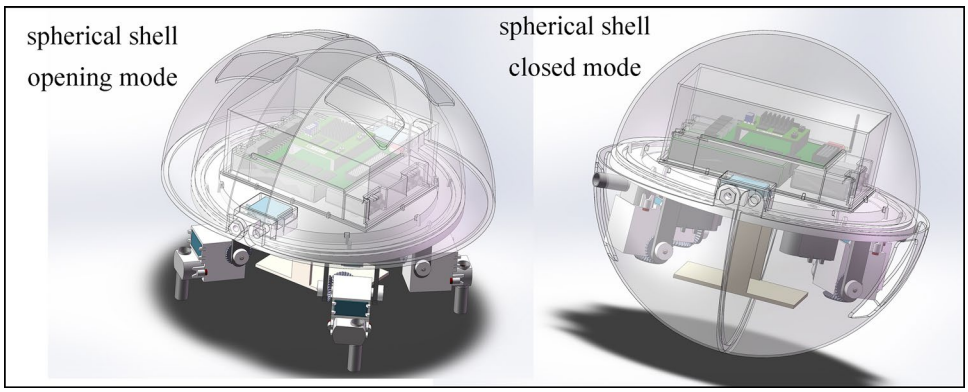

Fig. 7 Overall view of the new father robot

Our proposed amphibious spherical father robot is shown in Fig. 7. The movement mechanisms of the robot remain the same. When the amphibious spherical father robot walks on land, the lower spherical hemispherical is open and its four legs are vertically symmetrical. The image on the right shows the robot with the lower hemisphere closed. We assembled most parts by directly pushing them together; smaller parts were installed using the indented features generated by the grooves. This means of assembly greatly reduced the cumulative errors encountered during manual assembly: for the upper hemisphere, it not only saved space, but it also improved the waterproof performance (Shi et al. 2013b). Because the control system and other circuit boards, batteries, and some sensors are all in the upper hemisphere, and damage to these devices will seriously affect the robot's performance, it is important to ensure that the upper hemisphere shell is completely waterproof. Therefore, we adopted a double diaphragm waterproof platform for the upper hemisphere, as shown in Fig. 8.

This design ensured the soundness and integrity of the upper hemisphere shell. Compared with the previous version of the robot, which was assembled using many screws, the assembly of the new robot is more precise and stable. To further guarantee that the circuit boards and battery did not come into contact with water, we added a box without a top, which enabled us not only to pay attention to the battery and circuit boards, but also to greatly save space in the upper hemisphere and allow more compact connections between components. This integration of the structural design also enhanced the shock resistance and stability of the whole robot.

When walking, the four legs of the robot are subjected to a great deal of force, so the strength of the legs is very important. The leg structure consists mainly of a vertical motor, a horizontal motor, and a water-jet motor. We adopted integrated molding stents for the leg, considering that the structure of the leg must support the weight of objects in the upper hemisphere and the pressure imposed

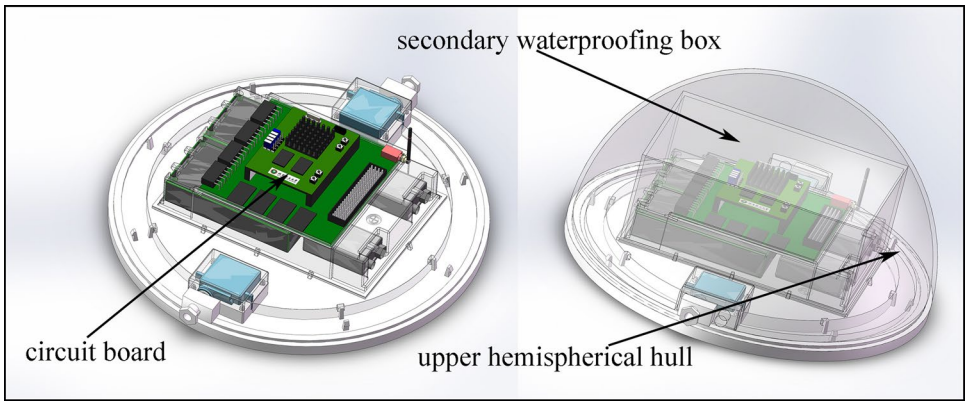

Fig. 8 *Upper hemisphere* of the new structure

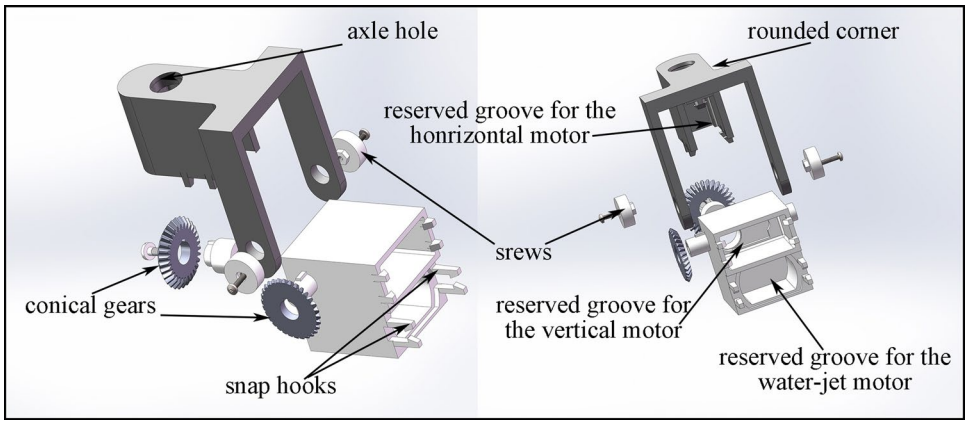

Fig. 9 Structure of the new leg

by the three lower motors to overcome the resistance and friction force while waking. We designed the leg structure as shown in Fig. 9. The leg brace joint was designed in a circular shape to increase the strength and compression performance of the scaffold. The front end of the stent was used to fix the upper circular plate and the horizontal motor. The groove used to load the horizontal motor was formed by an indentation. The front gear was used to fix the circular plate above and at the edge of the horizontal motor, with two spring buckles for further strengthening. We used a pair of conical gears to accelerate the movement of the legs.

3.2 Structural static analysis on land

While walking, the middle baffle plate is exposed to a relatively large force due to pressure from parts in the upper hemisphere, including the circuit boards, batteries, and shell, and due to the tension and moments generated by the legs. As described above, we used a double-diaphragm platform. The diameter of the first layer was 250 mm, and the thickness was 8 mm. We then added another platform with a thickness of 4 mm; this was divided into four parts to hold four batteries. The double-diaphragm platform is show in above mentioned image.

Considering that the weight of the robot was approximately 2.26 kg, we used an acrylonitrile butadiene styrene (ABS) plastic material. We simulated the appropriate pressure and forces acting on the plate; the results are shown in Fig. 10. The maximum displacement of the middle baffle plate was 2.462×10^{-6} m, the maximum nodal equivalent stress was 3.986 kPa, and the maximum elemental equivalent stress was 3.458 kPa. According to the nodal stress table, the maximum modal equivalent stress was 15, and the main stresses of this mode were $\sigma_1 = 1.463$ MPa, $\sigma_2 = -2.162$ MPa, and $\sigma_3 = -2.401$ MPa, which agrees with the third and fourth strength theory, as well as a standard check of our robot hemispherical shell and using Eqs. (1) and (2) (described in the next section). We checked the mechanical strength of the leg: because $[\sigma] = 22.73$ MPa, we obtained $\begin{cases} \sigma_{r3} = 3.865\text{MPa} < [\sigma] \\ \sigma_{r4} = 4.091\text{MPa} < [\sigma] \end{cases}$. Thus, the strength of the middle baffle plate met the third and fourth strength

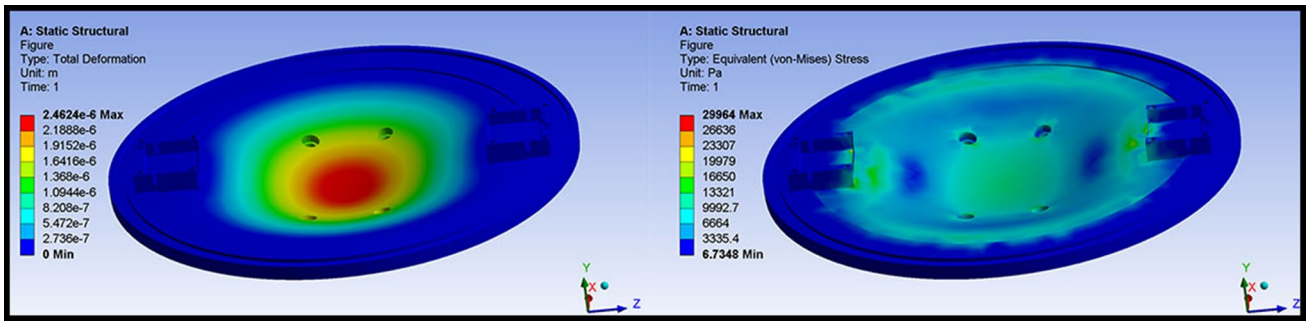

Fig. 10 Total displacement and equivalent stress

Fig. 11 Elements of the equivalent stress contour map

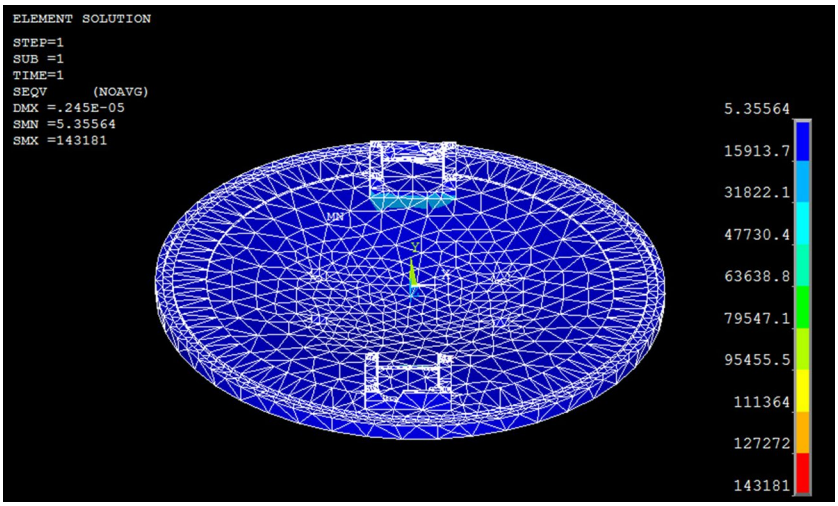

theory requirements, indicating that the structure is suitable for walking on land and swimming underwater. Therefore, the feasibility of the middle baffle plate structural design was improved. Simultaneously, elements of the equivalent stress contour map for the middle baffle plate is shows in Fig. 11. Figure 12 shows a nodal and stress and deformation contour map for the middle baffle plate.

The amphibious spherical father robot mainly uses its four legs to walk on different land environments, e.g., paving stones, cement floors, and grass, or in shallow water and underwater seabed environments. While walking, the leg brackets require more strength than the other parts because they are subjected to the force exerted by the upper hemisphere, such as the weight of the circuit boards, batteries, motors, and hemisphere shell, and to the axial force and moments from the fixed motor and leg structure, as well as resistance from the waterproof shell and the thruster.

For our analysis, we first imported the leg model from Solidworks into ANSYS software and established the local coordinate systems. We next applied pressure and steering forces, etc., to the leg structure. We neglected small-scale stresses and forces. Figure 13 shows the mesh model and the leg after the forces and moments were applied.

Next, we considered a static stress and deformation simulation analysis of the robot leg to verify its structural strength, considering that the weight of the robot is 2.26 kg. We included the ABS plastic material and used a scaffold thickness of 4 mm. The simulation results are shown in Fig. 14. The maximum total deformation of the legs was 2.6×10^{-5} m, and the maximum von Misses stress was 78.48 MPa. The intersection of two vertical planes was the area of stress concentration. Figure 15 shows a nodal and stress contour map for the leg: the maximum nodal and element stresses were 26.617 and 25.748 MPa, respectively. From Eqs. (1) and (2) (described in the next section), the middle plate strength design met the third and fourth strength theory requirements. Thus, the newly designed leg met our requirements: the leg was stable and feasible. Elements of the equivalent stress contour map for the leg is shows in Fig. 16.

3.3 Mechanical strength check of the spherical shell in water

We considered the complexity and uncertainty of the underwater environment, combined with the particular movement

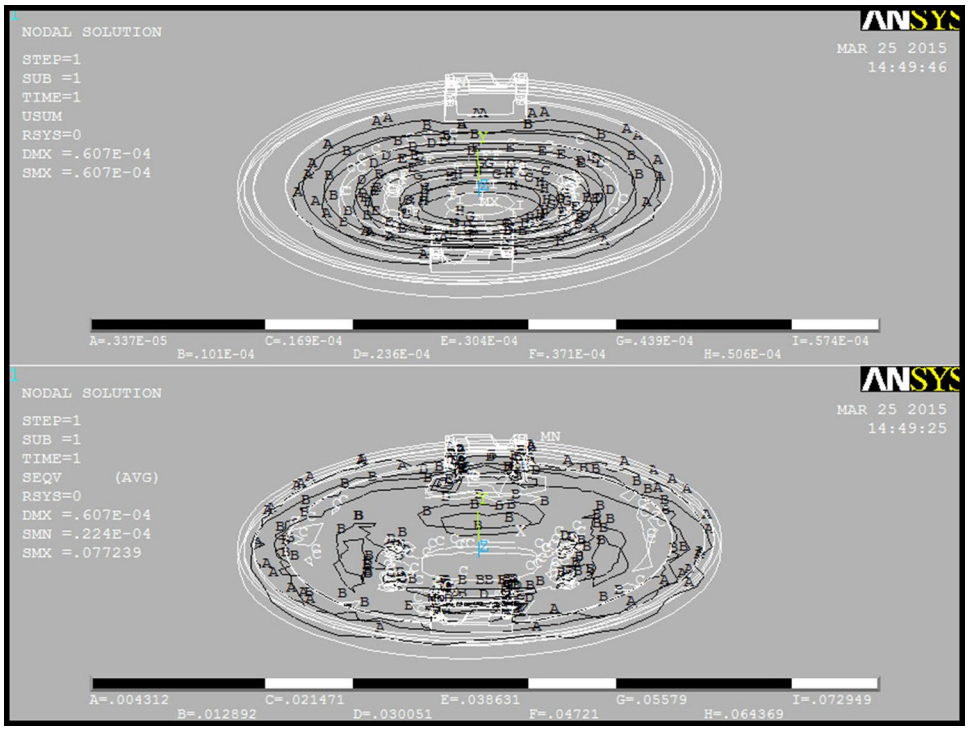

Fig. 12 Nodes of the equivalent stress and deformation contour map

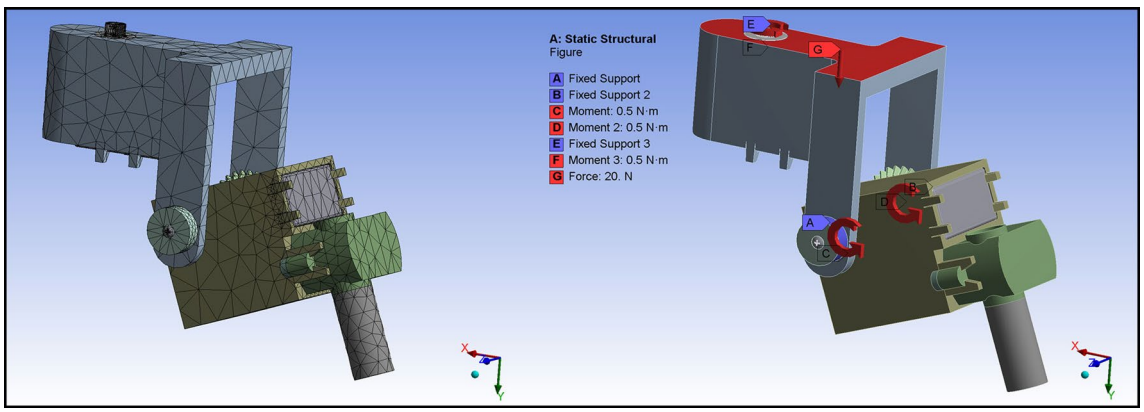

Fig. 13 Leg model mesh and forces

requirements of our amphibious spherical father robot. Because the robot control system and circuit boards, batteries, and sensors must not come into contact with water, the hemispherical shell must have sufficient strength to remain watertight. Therefore, we used 3D finite element modeling of the entire robot to analyze the exact structural performance of the shell. This allowed us to obtain the shell stress distribution and deformations for different seawater depths, and allowed us to calculate the maximum permissible water depth and verify the feasibility of the structural design. The results also provided support for further analysis of the structural strength and optimal design of the entire amphibious spherical father robot.

ANSYS has powerful analysis capabilities, but its 3D modeling capability is weak (Flynn et al. 2011; Pan et al. 2011). However, ANSYS provides a data interface program that can easily import models generated by other 3D software packages. We generated our amphibious spherical father robot structural model using Solidworks, and then imported the Solidworks model into ANSYS. Because the structure of our amphibious spherical father robot is complex, we simplified its 3D model by reducing the number of surfaces and parts to reduce computation time and obtain more effective results. Therefore, we removed some unimportant parts and surfaces, including

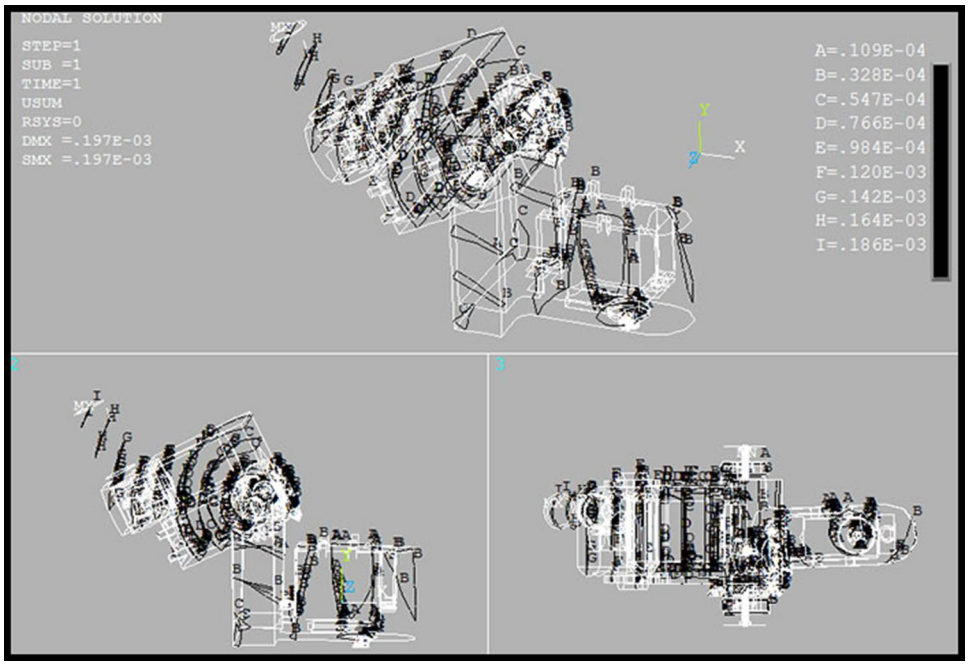

Fig. 14 Nodes of the total displacement contour map

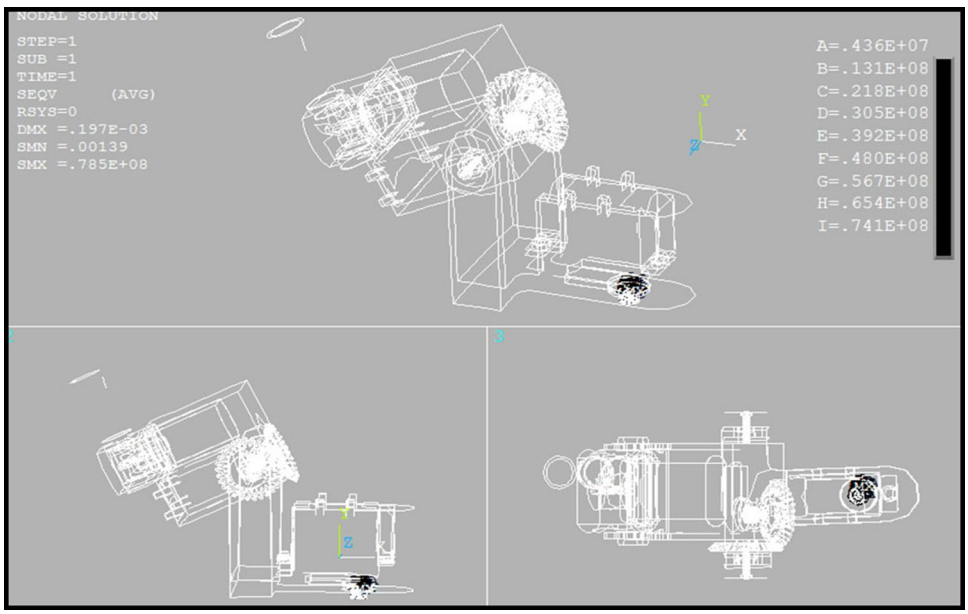

Fig. 15 Nodes of the equivalent stress contour map

screw threads, snap hook grooves, and the support frame for the servomotors. These parts were small and complicated, but had very little effect on the overall performance of the robot. We simplified the servomotors to a cubical shape and the water-jet thrusters to a cylindrical shape (Hama et al. 2003). Before importing the model, we performed a check to ensure that there was no interference between any parts. The simplified amphibious spherical father robot model imported into the ANSYS environment is shown in Fig. 17.

We used ABS plastic to help ensure that the hemispherical robot shell had sufficient strength. ABS is a high-strength plastic material, with good impact, heat, low-temperature, and chemical resistance, and excellent electrical properties. It is also relatively easy to process, handle, and model, and has the characteristics of dimensional

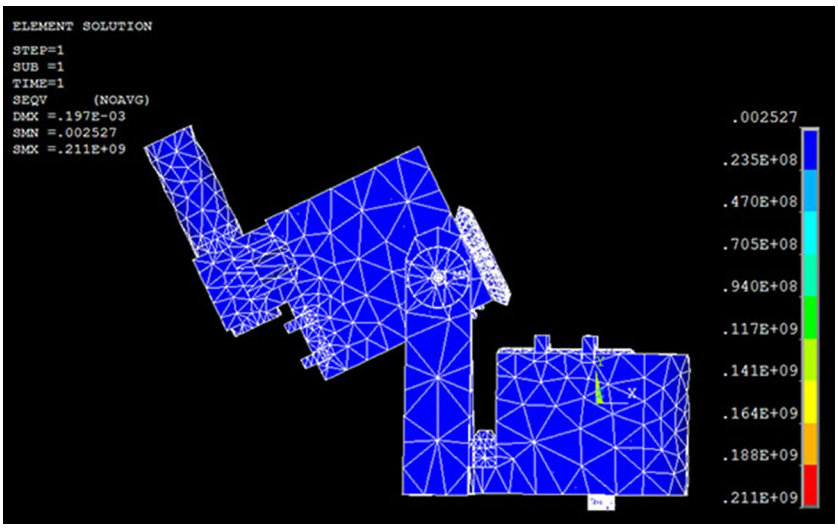

Fig. 16 Elements of the equivalent stress contour map

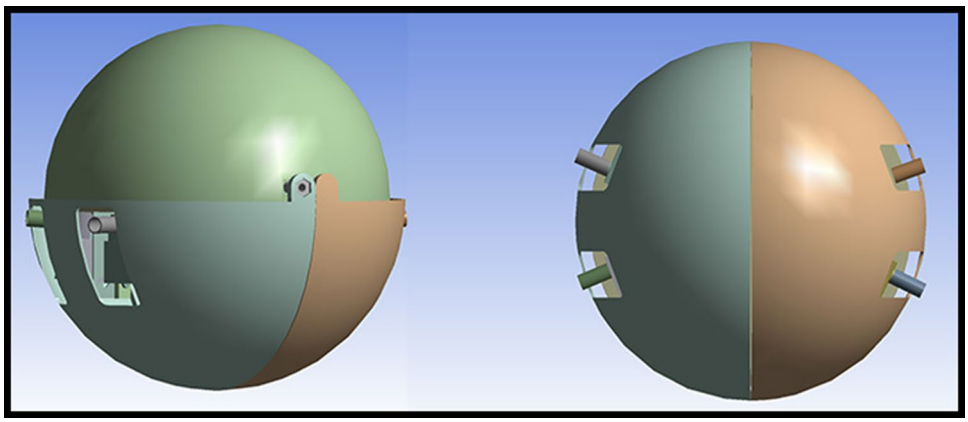

Fig. 17 Model of the amphibious *spherical* father robot shell

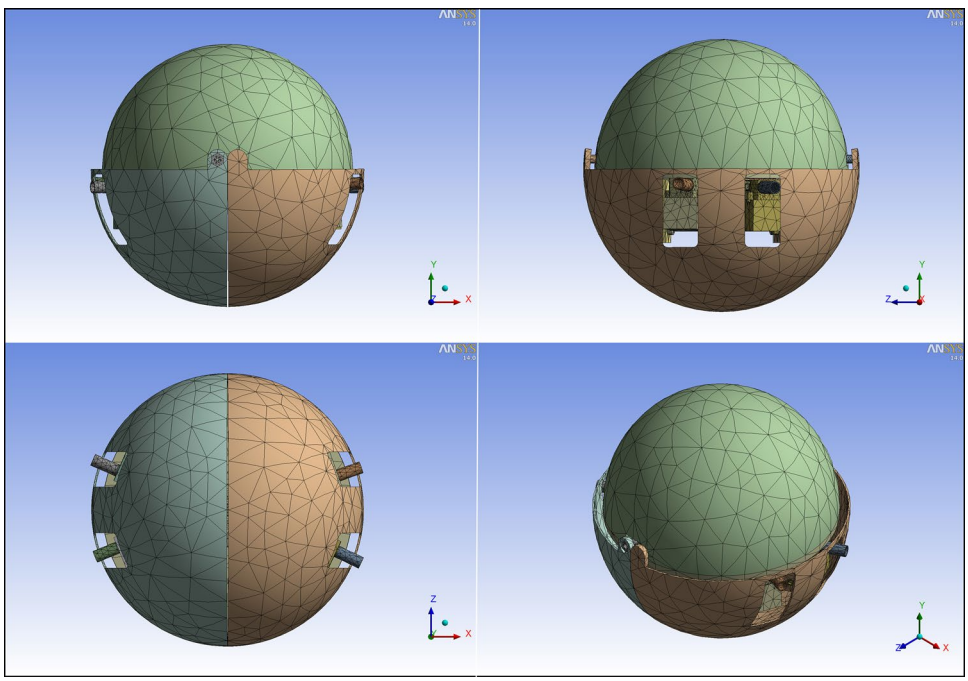

Fig. 18 Mesh model of the amphibious *spherical* father robot

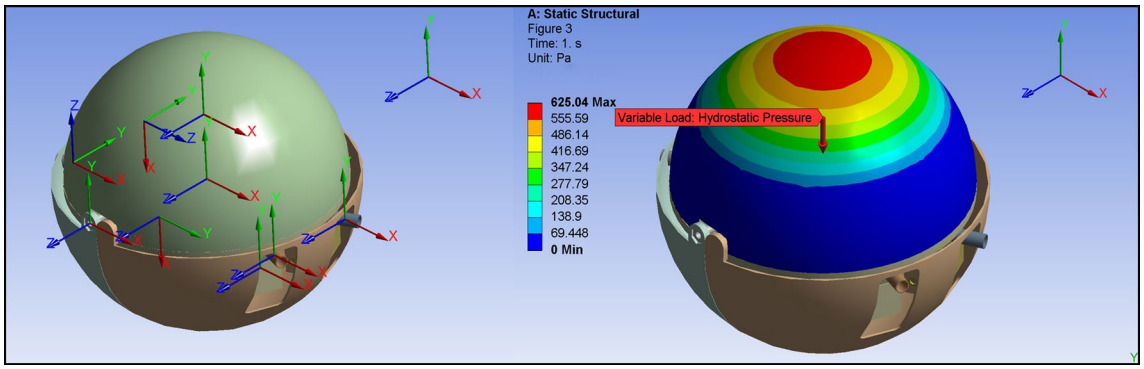

Fig. 19 Map after imposing the restraints and loads

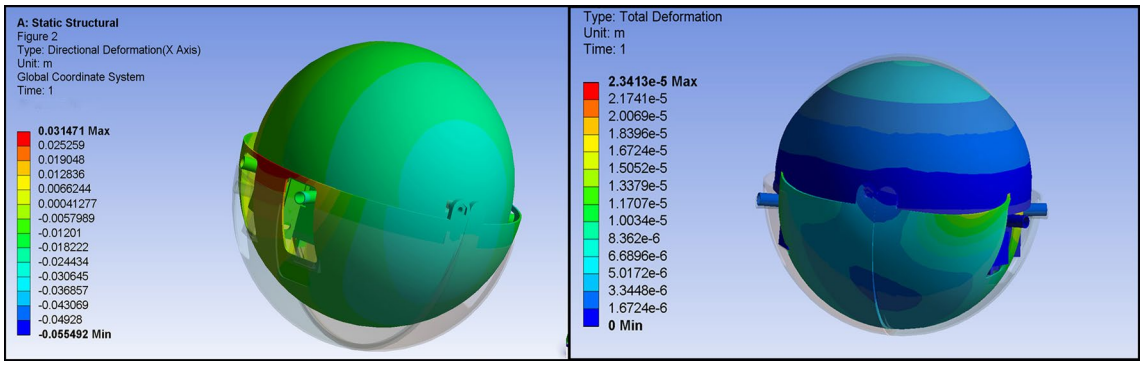

Fig. 20 Deformation shapes and undeformed contour map ($h = 2$ m)

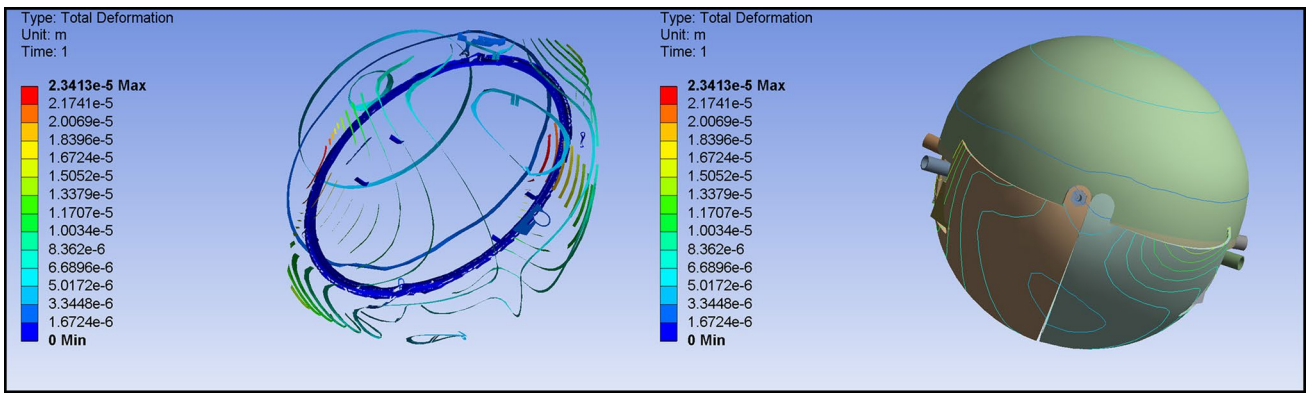

Fig. 21 Total displacement contour map ($h = 2$ m)

stability and surface gloss. Other ABS plastic parameters are described in the robot leg analysis above.

The finite element mesh is the most important factor in a numerical simulation analysis. The size of the mesh determines the performance of the finite element analysis and the computational complexity, and directly affects the accuracy of the results. ANSYS provides more than 200 types of elements that can be used to analyze a project. For a complex structure like our amphibious spherical father robot, the elements must be small to obtain good results. Therefore, we set the element size to 0.05 m, which gave us 1.5-million mesh elements. Figure 18 presents some

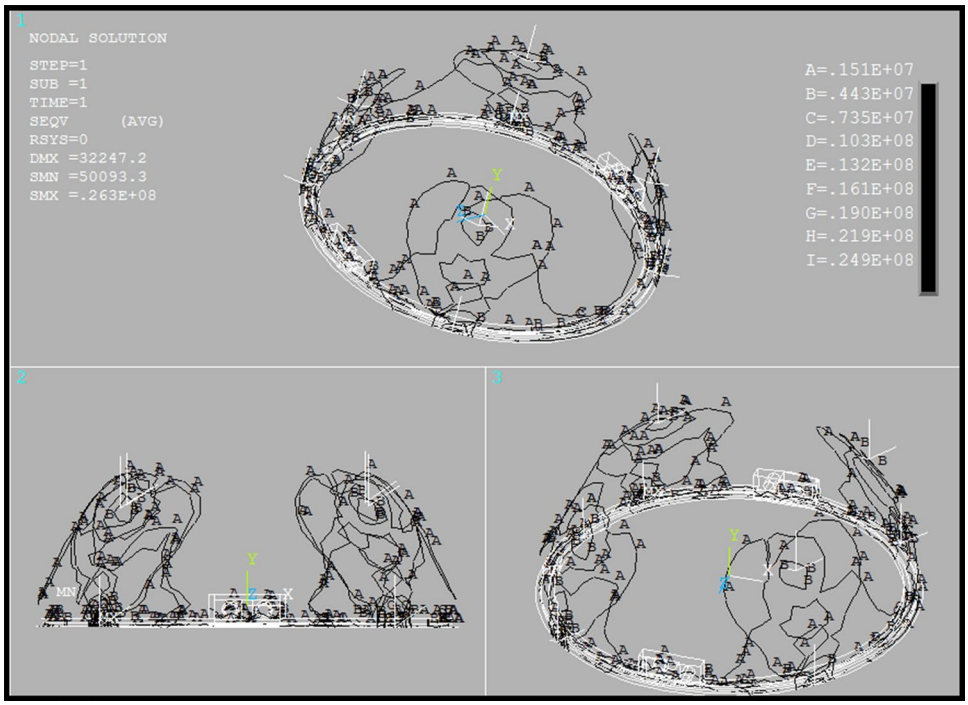

Fig. 22 Nodes of the equivalent stress contour map ($h = 2$ m)

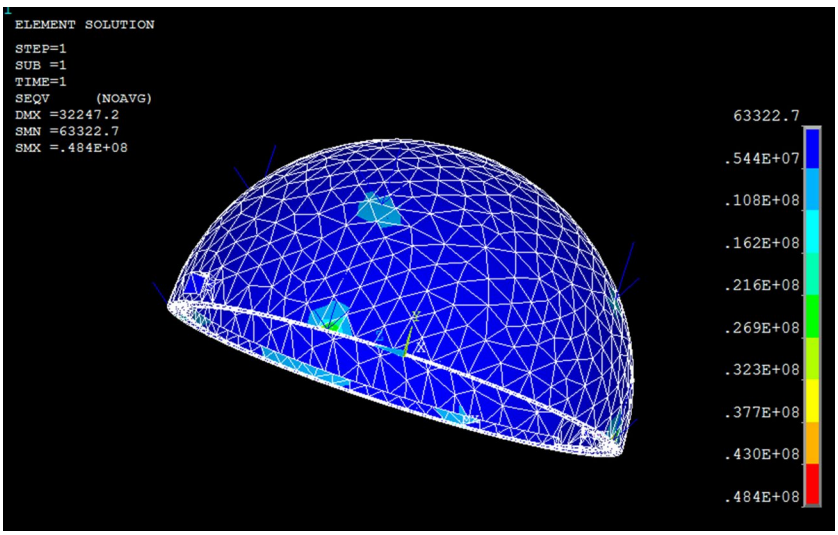

Fig. 23 Elements of the equivalent stress contour map ($h = 2$ m)

details of the mesh for the simplified robot shell. The mesh was generated using ANSYS Workbench. The total number of units was 20,941, and the total number of nodes was 67,505. Figure 19 shows the map after imposing the restraints and loads.

We selected a virtual non-uniform load corresponding to the robot under different hydrostatic pressures in the vertical and horizontal directions. However, we simplified the analysis by assuming that the shell was subjected to a uniform load in a seawater environment. The hydrostatic pressure as a function of seawater depth was calculated from $P = \rho g h$, where $\rho = 1025$ kg/cm^3 is the density of seawater, $g = 9.8$ m/s^2 is the acceleration of gravity, and h is the depth of the robot. We initially assumed $h = 5$ m, which gave $P = 50.23$ kPa. The direction of the load was perpendicular to the surface of the spherical father robot shell. Figure 19 shows a contour map obtained after imposing hydrostatic pressure restraints on our spherical robot shell.

We then considered $h = 2$ m. This yielded the displacements, stress map, nodal stresses, and elemental stresses shown in Figs. 20, 21, 22, 23. Figure 21 show that the maximum deformation of the robot shell was 2.341×10^{-5} m.

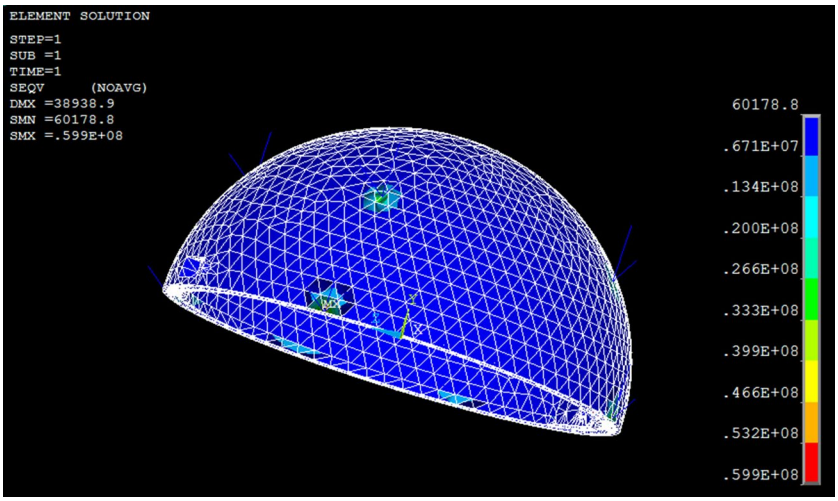

Fig. 24 Elements of the equivalent stress contour map ($h = 8$ m)

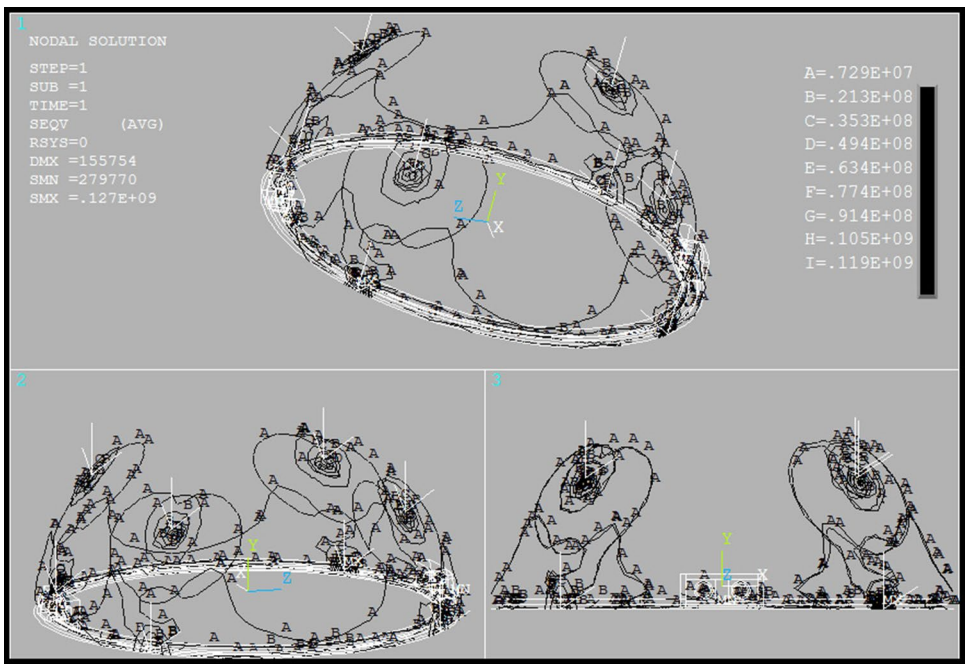

Fig. 25 Nodes of the equivalent stress contour map ($h = 8$ m)

Figures 22 and 23 show that the equivalent maximum stress and the corresponding nodal stress were 0.248 and 0.173×10^9 Pa, respectively.

For general machinery subjected to a static load, the safety factor for plastic material should be $n_s = 1.2$–2.5. Because ABS is plastic and the spherical robot moves in an underwater environment, and we only analyzed the stress when the robot was stationary, we used $n_s = 2.2$. There is no obvious yield limit for plastic, so we used the stress that produces 0.2 % plastic strain as a yield index:

$$[\sigma] = \frac{\sigma_s}{n_s} = \frac{\sigma_{0.2}}{n_s} = \frac{50}{2.2} = 22.73\text{MPa}$$

It is appropriate to use the maximum shearing stress theory (the third strength theory) and the distortion energy density theory (the fourth strength theory) to check the yield of carbon steel, copper, aluminum, and plastic. Therefore,

$$\sigma_{r3} = \sigma_1 - \sigma_3 \tag{1}$$

$$\sigma_{r4} = \sqrt{\frac{1}{2}\left[(\sigma_1 - \sigma_2)^2 + (\sigma_2 - \sigma_3)^2 + (\sigma_3 - \sigma_1)^2\right]} \tag{2}$$

We imported the analysis results from ANSYS Workbench into the ANSYS classic post-processor module interface, and used the command nodal solution in ANSYS for

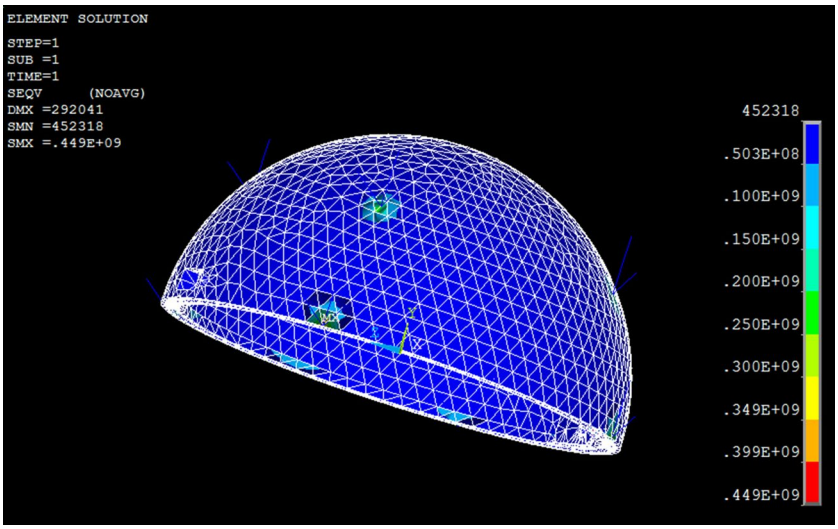

Fig. 26 Elements of the equivalent stress contour map ($h = 15$ m)

processing. We then conducted a series of related operations. The nodal stress output table indicated that the largest effective point was 4519. The principal stresses of the node were:

$$\sigma_1 = 6.602\text{MPa}$$
$$\sigma_2 = 4.517\text{MPa}$$
$$\sigma_3 = -4.358\text{MPa}$$

From Eqs. (1) and (2),

$$\begin{cases} \sigma_{r3} = 10.96\text{Mpa} < [\sigma] = 22.73\text{MPa} \\ \sigma_{r4} = 10.081\text{MPa} < [\sigma] = 22.73\text{MPa} \end{cases}$$

Consequently, the robot hemispherical shell satisfied the third and fourth strength theories, demonstrating that the shell was strong enough at seawater depths of 2 m. We repeated this analysis for seawater depths of 8 and 15 m, and checked the results using the above equations. The loads and constraints remained the same. The resulting stress diagrams are summarized in Figs. 24, 25, 26, 27, and the results are summarized in Table 1. Figures 24 and 25 show that the equivalent maximum stress and the corresponding nodal stress were 0.175 and 0.161 $\times$ 10^8 Pa, respectively. Figures 26 and 27 show that the equivalent maximum stress and the corresponding nodal stress were 0.329 and 0.302 $\times$ 10^8 Pa, respectively. The strength of the robot shell was sufficient up to seawater depths of 11 m. At depths greater than 11 m, the largest elemental equivalent stress was greater than the allowable stress of ABS material, and the robot shell was no longer strong enough. Here, we assumed that the robot was in seawater, which has a higher density than water, leading to more applied pressure. In fresh water, the robot would be able to reach deeper depths.

4 Conclusions

This paper extends on our group's previous publications about our amphibious spherical father–son robot system. This system of micro-structures can simultaneously achieve high mobility and high concealment, is independently recyclable, and has multi-functional movement modes, a high positional accuracy, stable flexible movements, a long cruising time and battery life, and a large loading capacity, as well as other characteristics. Therefore, it is suitable for future underwater applications in complex environments such as coral reefs and other narrow spaces.

Here, we described the structure of our proposed amphibious spherical father–son robot system, and the results of our experiments under various conditions. The results demonstrated that our amphibious spherical father robot can walk on different types of land, such as cement floors, paving stones, and grass, and in shallow water. It can implement forward motion, rotating motion, and floating/diving in an underwater environment. Thus, the robot can move in a practical manner.

In previous research, we improved our father robot by adding four passive wheels, and analyzed its movement mechanism. The results demonstrated that the redesigned structure had tremendous practicality and feasibility, except for some small instability phenomena. In this study, we redesigned the entire structure of the robot to improve its overall stability and ensure that it remains waterproof, and analyzed its structural strength. We also determined the maximum depth that can be tolerated by hemispherical robot shell. The newly designed amphibious spherical father robot met the designed strength requirements, and the hemispherical robot shell proved to be safe when the water depth was less than 11 m.

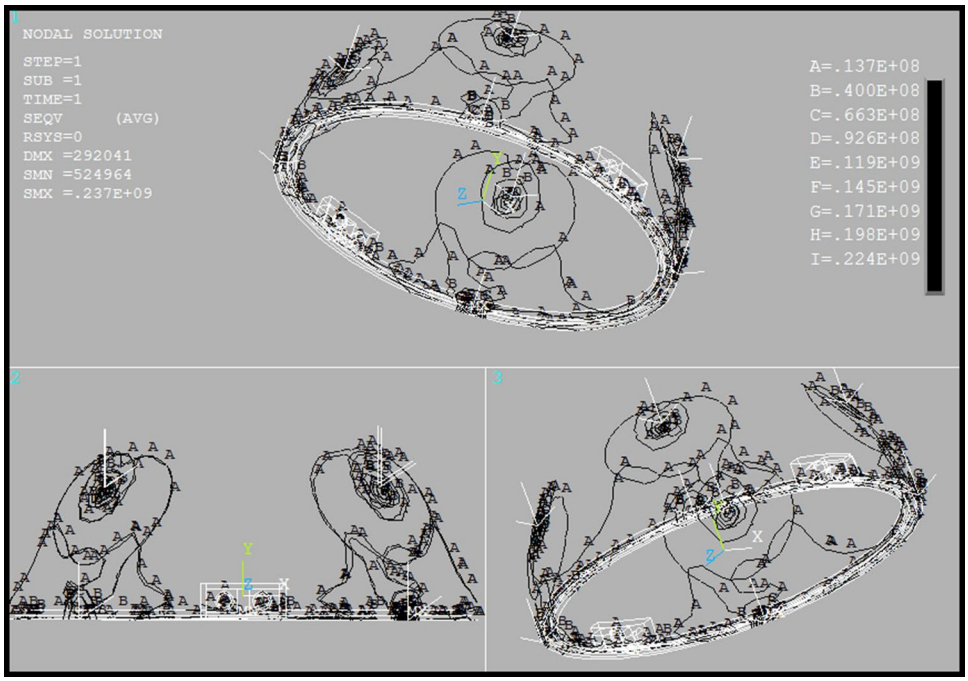

Fig. 27 Nodes of the equivalent stress contour map ($h = 15$ m)

Table 1 ANSYS mechanical analysis results

Depth (m)	Pressure (Pa)	Maximum displacement (m)	Maximum element of equivalent stress (Pa)	Maximum node of equivalent stress (Pa)
2	20,090	0.127E−04	0.438E+07	0.403E+07
5	50,225	0.110E−04	0.110E+08	0.110E+08
8	80,360	0.503E−04	0.175E+08	0.161E+08
10	100,450	0.628E−04	0.219E+08	0.202E+08
11	110,495	0.689E−04	0.241E+08	0.222E+08
12	120,540	0.752E−04	0.263E+08	0.242E+08
13	130,585	0.819E−04	0.285E+08	0.262E+08
14	140,630	0.881E−04	0.307E+08	0.282E+08
15	150,675	0.945E−04	0.329E+08	0.302E+08

Acknowledgments This work was supported by the Excellent young scholars Research Fund of Beijing Institute of Technology and the Basic Research Fund of the Beijing Institute of Technology (No. 3160012211405). This research project was also partly supported by National Natural Science Foundation of China (61375094), Key Research Program of the Natural Science Foundation of Tian-jin (13JCZDJC26200) and National High Tech. Research and Development Program of China (No. 2015AA043202).

References

Abdulsadda A, Tan X (2012) An artificial lateral line system using IPMC sensor arrays. Int J Smart Nano Mater 3(3):226–242

Behkam B, Sitti M (2006) Design methodology for biomimetic propulsion of miniature swimming robots. J Dyn Syst Meas Control 128(1):36–43

Brunetto P, Fortuna L, Graziani S, Strazzeri S (2008) A model of ionic polymer-metal composite actuators in underwater operations. Smart Mater Struct 17(2):1–12. Art ID 025029

Chen W, Dong Y, Zhu Q, Li B (2010) Finite element analysis of three-dimensional robot tactile sensors based on PVDF. Chin J Sens Actuators 23(3):336–340

Flynn C, Taberner A, Nielsen P (2011) Mechanical characterisation of in vivo human skin using a 3D force-sensitive micro-robot and finite element analysis. Biomech Model Mechanobiol 10(1):27–38

Guo S, Shi L, Xiao N, Asaka K (2012a) A biomimetic underwater microrobot with multifunctional locomotion. Robot Auton Syst 60(12):1472–1483

Guo S, Shi L, Mao S, Li M (2012b) Design and kinematic analysis of an amphibious spherical robot. In: Proceedings of 2012 IEEE international conference on mechatronics and automation. IEEE, Chengdu, 5–8 Aug 2012, pp 2214–2219

Ha NS, Goo NS (2010) Propulsion modeling and analysis of a biomimetic swimmer. J Bionic Eng 7(3):259–266

Hama T, Asakawa M, Fuchizawa S, Makinouchi A (2003) Analysis of hydrostatic tube bulging with cylindrical die using static explicit FEM. Mater Trans 44(5):940–945

He Y, Guo S, Shi L (2014) 3D Printing technology-based an Amphibious Spherical Underwater Robot. In: Proceedings of 2014 IEEE international conference on mechatronics and automation. IEEE, Tianjin, 3–6 Aug 2014, pp 1382–1387

Heo S, Wiguna T, Park HC, Goo NS (2007) Effect of an artificial caudal fin on the performance of a biomimetic fish robot propelled by piezoelectric actuators. J Bionic Eng 4(3):151–158

Li Y, Guo S, Yue C (2014) "Preliminary concept and kinematics simulation of a novel spherical underwater robot". Proceedings of 2014 IEEE International Conference on Mechatronics and Automation, Tianjin, 3–6 Aug 2014, pp 1907–1912

Lin X, Guo S (2012) Development of a spherical underwater robot equipped with multiple vectored water-jet-based thrusters. J Intell Rob Syst 67(3–4):307–321

Lin X, Guo S, Tanaka K, Hata S (2010) Development and evaluation of a vectored water-jet-based spherical underwater vehicle. INFORMATION: Int Interdiscip J 13(6):1985–1998

Liu W, Jia X, Wang F, Jia Z (2010) An in-pipe wireless swimming micro-robot driven by giant magnetostrictive thin film. Sens Actuators A 160(1–2):101–108

Mori M, Hirose S (2006) Locomotion of 3D snake-like robots-shifting and rolling control of active cord mechanism ACM-R3. J Robot Mechatron 18(5):521–528

Najem J, Sarles SA, Akle B, Leo DJ (2012) Biomimetic jellyfish-inspired underwater vehicle actuated by ionic polymer metal composite actuators. Smart Mater Struct 21(9):1–11. Art ID 094026

Pan Y, Guo M, Li W (2011) Mechanical property analysis of automatic teller machines based on ANSYS. J Mach Des 28(1):60–63

Shi L, Guo S, Asaka K (2011) Development of a new jellyfish-type underwater microrobot. Int J Robot Autom 26(2):229–241

Shi L, Guo S, Asaka K (2012a) A novel jellyfish- and butterfly-inspired underwater micro robot with pectoral fins. Int J Robot Autom 27(3):276–286

Shi L, Guo S, Li M, Mao S, Xiao N, Gao B, Song Z, Asaka K (2012b) A novel soft biomimetic microrobot with two motion attitudes. Sensors 12(12):16732–16758

Shi L, Guo S, Mao S, Li M, Asaka K (2013a) Development of a lobster-inspired underwater microrobot. Int J Adv Robot Syst 10(44):1–15. doi:10.5772/54868

Shi L, Guo S, Mao S, Yue C, Li M, Asaka K (2013b) Development of an amphibious turtle-inspired spherical mother robot. J Bionic Eng 10(4):446–455

Shi L, He Y, Guo S (2013c) IPMC Actuator-based a Movable Robotic Venus Flytrap. In: Proceedings of 2013 ICME international conference on complex medical engineering. IEEE, Beijing, 25–28 May 2013, pp 375–378

Shi L, He Y, Guo S (2013d) Skating motion analysis of the amphibious quadruped mother robot. In: Proceedings of 2013 IEEE international conference on mechatronics and automation. IEEE, Takamatsu, 4–7 Aug 2013, pp 1749–1754

Villanueva A, Joshi K, Blottman J, Priya S (2010) A bio-inspired shape memory alloy composite (BISMAC) actuator. Smart Mater Struct 19(2):1–17(025013)

Wang Z, Hang G, Li J, Wang Y, Xiao K (2008) A micro-robot fish with embedded SMA wire actuated flexible biomimetic fin. Sens Actuators A 144(2):354–360

Wang W, Chao G, Niu J (2011) Design and finite-element analysis of robotic fish sealing tank. Lubr Eng 36(12):80–84

Zhang Z, Wang S, Tan M (2004) 3-D locomotion control for a biomimetic robot fish. J Control Theory Appl 2(2):169–174

Zhang W, Guo S, Asaka K (2006) A new type of hybrid fish-like micro robot. Int J Autom Comput 3(4):358–365